applied sciences

Article

A Combined Artificial-Intelligence Aerodynamic Design Method for a Transonic Compressor Rotor Based on Reinforcement Learning and Genetic Algorithm

Xiaohan Xu, Xudong Huang *, Dianfang Bi and Ming Zhou

School of Aerospace Engineering, Tsinghua University, Beijing 100084, China
* Correspondence: xdhuang@tsinghua.edu.cn

Abstract: An aircraft engine's performance depends largely on the compressors' aerodynamic design, which aims to achieve higher stage pressure, efficiency, and an acceptable stall margin. Existing design methods require substantial prior knowledge and different optimization algorithms to determine the 2D and 3D features of the blades, in which the design policy needs to be more readily systematized. With the development of artificial intelligence (AI), deep reinforcement learning (RL) has been successfully applied to complex design problems in different domains and provides a feasible method for compressor design. In addition, the applications of AI methods in compressor research have progressively developed. This paper described a combined artificial-intelligence aerodynamic design method based on a modified deep deterministic policy gradient algorithm and a genetic algorithm (GA) and integrated the GA into the RL framework. The trained agent learned the design policy and used it to improve the GA optimization result of a single-stage transonic compressor rotor. Consequently, the rotor exhibited a higher pressure ratio and efficiency owing to the sweep feature, lean feature, and 2D airfoil angle changes. The separation near the tip and the secondary flow decreased after the GA process, and at the same time, the shockwave was weakened, providing improved efficiency. Most of these beneficial flow field features remained after agent modification to improve the pressure ratio, showing that the policy learned by the agent was generally universal. The combination of RL and other design optimization methods is expected to benefit the future development of compressor designs by merging the advantages of different methods.

Keywords: reinforcement learning; genetic algorithm; turbomachinery; design; optimization

check for updates

Citation: Xu, X.; Huang, X.; Bi, D.; Zhou, M. A Combined Artificial-Intelligence Aerodynamic Design Method for a Transonic Compressor Rotor Based on Reinforcement Learning and Genetic Algorithm. *Appl. Sci.* **2023**, *13*, 1026. https://doi.org/10.3390/app13021026

Academic Editor: Florent Ravelet

Received: 9 December 2022
Revised: 7 January 2023
Accepted: 8 January 2023
Published: 12 January 2023

1. Introduction

The compressor is one of the most critical components in an aero engine, exhibiting viscous, compressible, and unsteady flow. In previous studies on transonic axial compressors [1], considerable efforts have been spent on improving the stage pressure ratio, efficiency, and stability margin. Historically, research about axial compressor design relied on empirical data correlations, and then the through-flow methods were proposed [2,3]. Over the past two decades, computational fluid dynamics (CFD) has played a dominant role [3], while empirical information is still needed.

Using CFD, researchers have efficiently analyzed the complex 3D compressor flow field [4]. A great deal of previous research has applied CFD tools with the Reynolds-averaged Navier-Stokes (RANS) equations [4,5] because of the computational resource limitation. As a result of the computational capability improvement, several studies have emerged to evaluate the multistage and unsteady case [4].

A large and growing amount of the literature has investigated the optimization of compressors [6], including two main kinds of methods [7]: stochastic and gradient-based methods. The genetic algorithm (GA), a widely used stochastic method, has been successfully applied since the 2000s [8,9]. Using the advanced NSGA-II algorithm [10], the pressure ratio, efficiency, and operating range of single-stage transonic axial compressors were improved in several cases [11,12]. Ma et al. [13] compared particle swarm optimization (PSO) [14], GA, and a hybrid PSO-GA algorithm, then suggested that the hybrid PSO-GA algorithm performed best in a centrifugal compressor. In another aspect, several studies [15,16] have used gradient-based algorithms in turbomachinery and focused on improving the efficiency and pressure ratio. Generally, better compressors can be found by optimization at certain constraints and objective settings; those studies outline a critical role for optimization in compressor design.

One limitation of the above optimization methods is that their results cannot directly guide design; prior knowledge of the designers is needed, especially when the designs need to be modified frequently in a multidisciplinary or engineering context. Learning the design policy becomes possible with the development of reinforcement learning (RL) methods [17], which train the machine to learn the design like humans. In the past few years, RL methods have been used to successfully solve many complex design problems, including designing personalized therapies [18], designing proteins [19], and even finding matrix multiplication algorithms [20].

There are relatively few studies attempting to apply RL in aerodynamic design, focusing mainly on 2D airfoils for easier CFD analysis. Several deep RL algorithms [21] have been developed for a continuous state space, corresponding to the design space of compressors. Some authors have considered the usage of 2D external flow airfoils. A recent study by Viquerat et al. [22] involved an application of proximal policy optimization (PPO) [23], which maximized the lift-to-drag ratio by exploring the design space. Similarly, Li [24] also used PPO to minimize the drag of a supercritical airfoil. In the turbomachinery field, internal flow airfoils have also been considered. Qin [25] demonstrated that the total pressure loss could be reduced by modifying the 2D airfoil via a trained agent using a deep deterministic policy gradient (DDPG) [26]. These studies clearly indicated that RL methods could successfully learn the design policy of 2D airfoils and improve aerodynamic performance. However, no corresponding attempts for the 3D rotor case have been found to date.

Different applications of machine learning methods exist in the literature regarding turbomachinery research. Much of the previous research on compressor optimization established the artificial neural network and its variations as surrogate models (such as [13,16]). Another idea was proposed by Li et al. [27], where a deep convolutional generative adversarial network was trained to generate airfoils using existing airfoils. For the CFD solver itself, machine learning methods can improve the model accuracy of the RANS equations with a lower computational cost than LES and DNS, according to the summary by Hammond et al. [28,29], but still cannot fully replace conventional methods. Altogether, these studies indicate that machine learning methods can improve turbomachinery analysis and optimization from different aspects.

The RL and GA methods have their own frameworks and features. The trained agents in RL modified the geometries to change the performance with continuous steps, while the GA process generated a Pareto front that has no relation with other cases in the design space and was considered a one-step process. This paper proposed integration of the RL method and GA for the aerodynamic design of a transonic axial compressor with modified DDPG and NSGA-II algorithms. The policy for improving the pressure ratio was learned by the agents and used to modify the result of the GA, improving its pressure from lower to higher than the reference. The remainder of this paper is organized as follows: Section 2 illustrates methods to analyze the rotor, establish the modified DDPG algorithm with surrogate models, and implement NSGA-II in this context. As described in Section 3, the agents were trained in the RL environment to learn the design policies, and the GA process generated the Pareto front. Then, cooperation was implemented by integrating the GA process into the RL framework. Section 4 discusses the mechanism of improvement, the details of the flow field, and the computational resource cost.

2. Methods

The compressor aerodynamic design was considered a Markov decision process (MDP) [17], so different design and optimization methods were considered steps in the MDP and integrated into the RL framework. Figure 1 shows the overall structure of the methods, where surrogate models were applied to reduce the computational cost of CFD. The RL agent interacted with the environment by giving an action a_t according to the design variables s_t of step t. Then, the environment generated r_t and s_{t+1}, determined only by s_t and a_t. The GA process reused the RL environment to calculate the fitness functions of individuals and output the result case from the final pop. The results of the RL agents, GA process, and cooperative result after modification by the trained agents were checked by CFD directly.

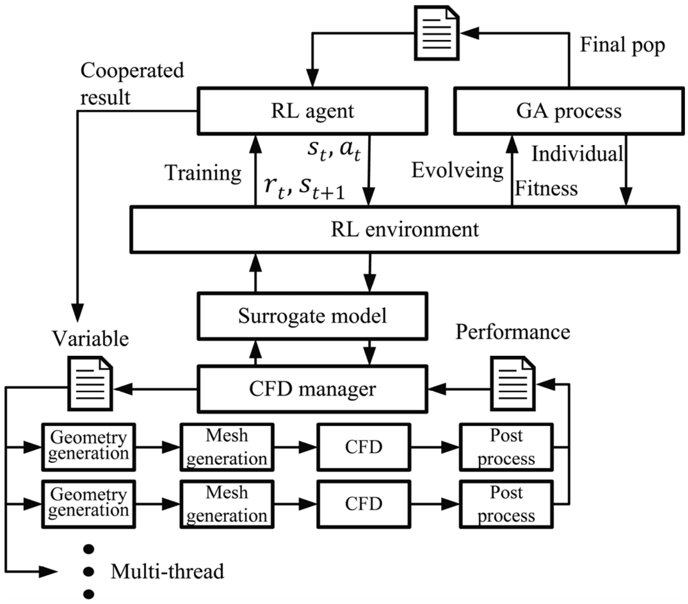

Figure 1. Overall structure of the artificial intelligence design framework, with a hierarchical structure. The CFD manager calculates the operating characteristics of rotors in multiple threads, extracts the performance, and manages the data.

2.1. CFD Method

2.1.1. CFD Tools

The commercial software package NUMECA 14.1 was selected for CFD analysis, in which AutoGrid generated an O-H structured grid from the rotor geometry and Fine Turbo solved the 3D RANS equations. After the calculation was finished, NUMECA CFView completed the postprocessing. All tools were automatically driven by the scripts.

The viscous and inviscid fluxes were determined using second-order Jameson-type dissipation, and an explicit Runge–Kutta scheme was applied for time discretization. The Spalart–Allmara (S–A) model was selected to close the RANS equation. As one of the most successful one-equation turbulence models, the S-A model performs well in the boundary layer and pressure gradient area, so it is widely used to predict complex flows with separation, showing attractiveness in turbomachinery analysis. Moreover, the S-A model in NUMECA has been widely validated and applied [30–32], and it consumes less additional CPU and memory than the k–ε model.

2.1.2. Rotor 67 Simulation

NASA Rotor 67 [33] is a low-aspect-ratio transonic axial-flow fan rotor with experimental data that was used as the reference design. Table 1 shows the primary features of Rotor 67. Note that the observed tip clearance was 0.061 cm rather than the designed value of 0.101 cm [33].

Table 1. Specifications of Rotor 67 [33].

Parameter	Value	Parameter	Value
Rotational speed (rpm)	16,043	Relative tip Mach number	1.3
Tip clearance (cm)	0.101	Mass flow rate (kg/s)	33.25
Number of blades	22	Pressure ratio	1.63

Different grids were calculated, with node numbers of 0.8 M, 1.2 M, 1.6 M, and 2.0 M. The setting $y^+ = 1$ was specified for all grids, and the 1.2 M grid was shown in Figure 2. The calculated operating characteristics and the experimental results are plotted in Figure 3. The pressure ratio and efficiency fit the experimental data well for the medium (1.2 M) and fine (1.6 M and 2.0 M) meshes, while the coarse mesh deviated from the experimental values. The calculated chock mass flow rate was 34.3 kg/s, slightly less than the experimental value and considered acceptable.

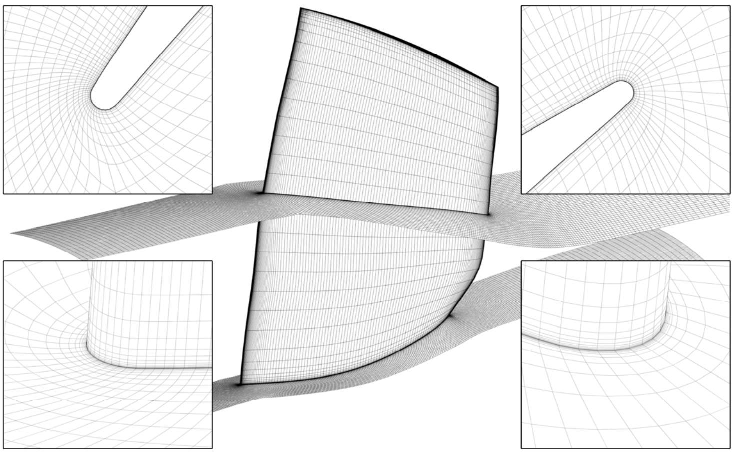

Figure 2. The multiblock structured O–H grid with 1.2 M nodes.

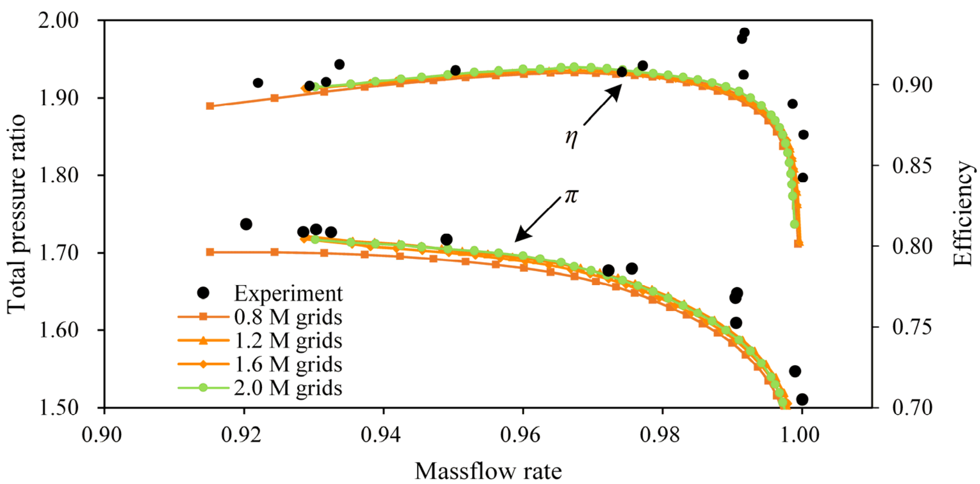

Figure 3. Operating characteristics of NASA Rotor 67 with 0.8 M, 1.2 M, 1.6 M, and 2.0 M grids.

Physically, rotating stall is an unsteady process, but the rotor was analyzed at steady state. Thus, some of the time-averaged features or convergence criteria could approximately indicate the 'numerical stall point' [15,34,35]. The calculation was considered converged if the adiabatic efficiency variation was less than 0.04% per 100 iterations and was regarded as stalled if it did not converge. The calculated stall mass flow was about 93% for the grids with 1.2 M, 1.6 M, and 2.0 M nodes. Due to the insufficient special resolution, CFD cases with 0.8 M grid were harder to diverge and obtained a lower stall mass flow rate numerically. Moreover, the pressure ratio and efficiency were also changed since the 0.8 M grid captured fewer flow details. The near stall mass flow rate and the pressure ratio at $\dot{m} = 0.97$ of different grids were plotted in Figure 4, showing that the results changed only slightly at grid numbers larger than 1.2 M. Thus, the grid independency was acceptable, and the 1.2 M grid was selected. The shock wave structure of different spans is shown in Figure 5. The calculated shock wave showed similar features to the experiment [33]. An oblique shock wave was identified at the leading edge of the blades, and normal shock waves were found in the passages.

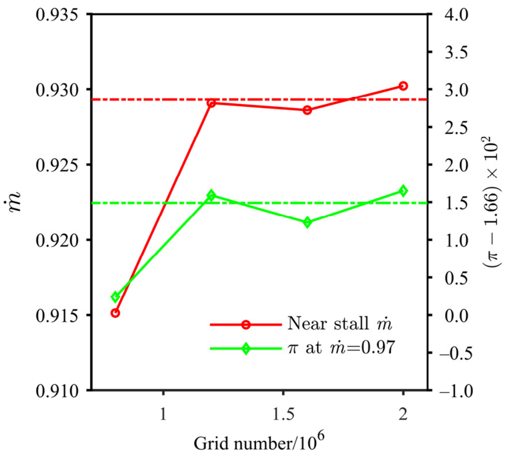

Figure 4. The near stall mass flow rate and the pressure ratio at $\dot{m} = 0.97$.

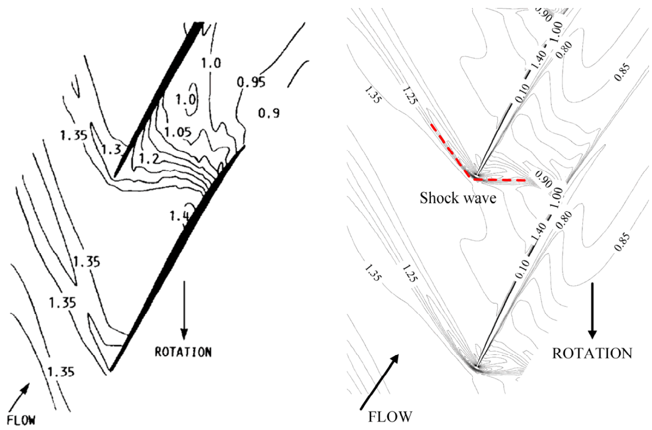

(**a**)

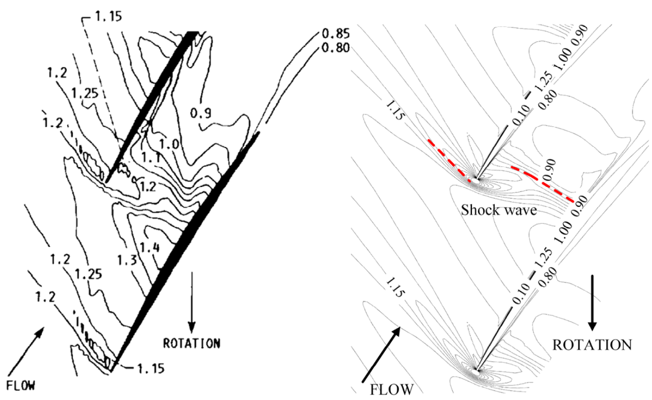

(**b**)

Figure 5. Relative Mach number distribution of the experimental [33] and CFD results: (**a**) 90% span of the experimental (left) and simulated (right) results; (**b**) 70% span of the experimental (left) and simulated (right) results. Red dotted line is to denote the shock wave.

The pressure ratio and temperature ratio distributions of the near-peak efficiency are plotted in Figure 6. The CFD results fit the experimental results well. The CFD tools and methods were confirmed to give suitable results and were then applied to generate and evaluate the rotor geometries generated by agents.

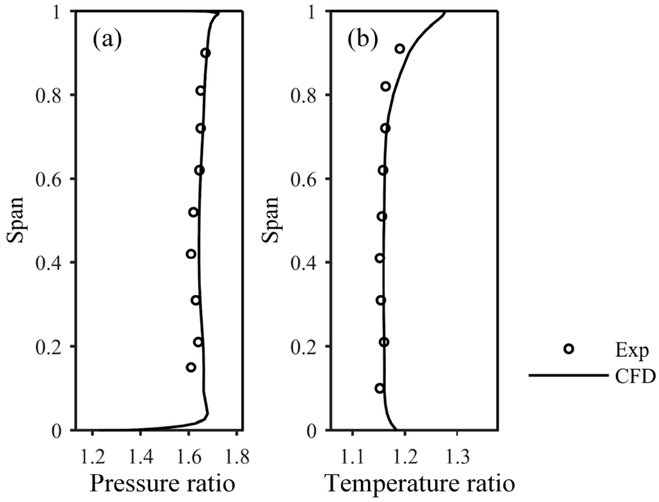

Figure 6. Variable distributions in the span of the experiment [33] and CFD: (**a**) pressure distribution in the span; (**b**) temperature distribution in the span.

2.1.3. Rotor Performance

The most notable performance metrics of a compressor are the mass flow $\dot{m}$, pressure ratio π, efficiency η, and stability margin SM extracted from the operating characteristic curve. The back pressure p_{out} was changed according to a geometric progression distribution, decreasing the pressure interval near the stall pressure. A typical operating characteristic curve generated by CFD is shown in Figure 7. The peak efficiency point was selected as the working point, and then the mass flow $\dot{m}_W$, pressure ratio π_W, and efficiency η_W were determined.

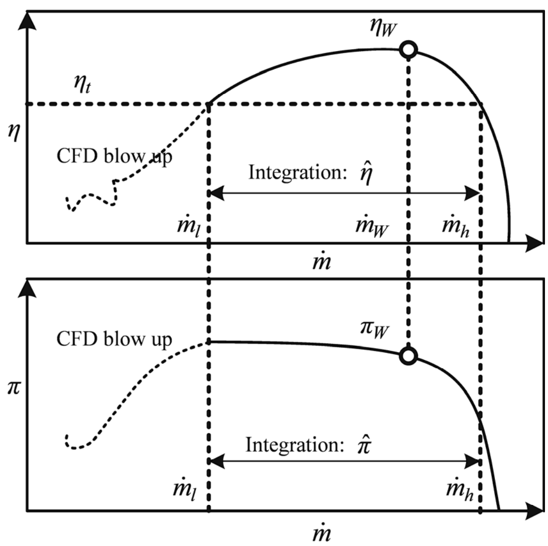

Figure 7. Typical operating characteristics calculated by CFD, with the definition of 7 selected performance variables.

Furthermore, several variables were defined to evaluate the whole operating characteristic curve generated by CFD. A range of satisfactory efficiency $[\dot{m}_l, \dot{m}_h]$ was defined after setting an efficiency threshold η_t, as shown in Figure 7. The criteria involved the numerical stall feature of the rotors, so these criteria were used to replace the exact stall point when training agents, saving computational resources.

Then, the integral efficiency $\hat{\eta}$ and pressure ratio $\hat{\pi}$ were expressed as shown in Equations (1) and (2) to indicate the efficiency and pressure ratio of the whole operating characteristic curve, respectively. The rotor performance was ultimately described by 7 dimensions, denoted by $p_i \in \mathbb{P} = \{\dot{m}_l, \dot{m}_h, \hat{\eta}, \hat{\pi}, \dot{m}_W, \pi_W, \eta_W\}$, $i = 1, 2, \ldots, 7$.

$$\hat{\eta} = \frac{\int_{\dot{m}_l}^{\dot{m}_h} \eta(\dot{m}) d\dot{m}}{\dot{m}_h - \dot{m}_l} \tag{1}$$

$$\hat{\pi} = \frac{\int_{\dot{m}_l}^{\dot{m}_h} \pi(\dot{m}) d\dot{m}}{\dot{m}_h - \dot{m}_l} \tag{2}$$

2.2. RL Components

2.2.1. Rotor Parameterization

A parameterization generator was built to generate the rotor geometry. Design variables were defined to generate the 3D features and the distribution of 2D parameters of different spanwise locations, and then the 3D rotor blade was staked by 2D airfoils.

Eighteen geometric parameters were selected to be design variables and generate the span distribution of geometric features using 3rd-order Bezier curves. The reference values were extracted from the original NASA Rotor 67 geometry, which also provided the lower and upper bounds.

2.2.2. Surrogate Model

The surrogate model gives a relatively accurate approximation of CFD analysis with a much lower computational cost, thus accelerating the design process. This work used kriging models [36] to approximate the rotor performance because this approach needs fewer sample points, even in high-dimensional design space. Moreover, the sample points were determined by the maximin Latin hypercube design [37]. Finally, seven separate kriging models were trained to approximate the rotor performance.

$$p_i' = p_{i,max} + \frac{1}{a_p} \ln(a_p \frac{p_{i,max} - p_i}{p_{i,max} - p_{i,min}} + 1) \times (p_{i,max} - p_{i,min}) \tag{3}$$

The error reduction process successfully enhanced the kriging model's performance and reduced the necessary sample number by restricting the influence of the few poor sample points. In Equation (3), the parameter a_p indicated the strength of the restriction, with the performance $p_i \in \mathbb{P}$ decreasing if this parameter exceeded the reasonable range $[p_{i,min}, p_{i,max}]$. The reasonable range was determined according to p_i distributions in sample points, guaranteeing that most of the restriction occurred on the side that did not influence the expected performance. The reconstructed restricted performance p_i' has the same monotonicity and first-order smoothness.

Different combinations of hyperparameters were applied to determine surrogate models, with error reduction parameter $a_p \in \{0, 3, 5\}$, sample points $N > 300$, and parameters of the kriging model $P_{min} = \{1.3, 1.5, 1.7\}$ and $\theta_{max} = \{10, 30\}$. The surrogate models were trained in the different number of sample points and other parameter combinations, as shown in Figure 8. Since the surrogate models had been trained in different sample point sets and several times, the results were regarded as consistent. Then, the surrogate models of each p_i with the best coefficient of determination R^2 were selected as shown in Table 2, where the mean absolute error (MAE) was also listed. The surrogate models were accurate enough to predict the rotor performance, so the RL environment was established based on these surrogate models.

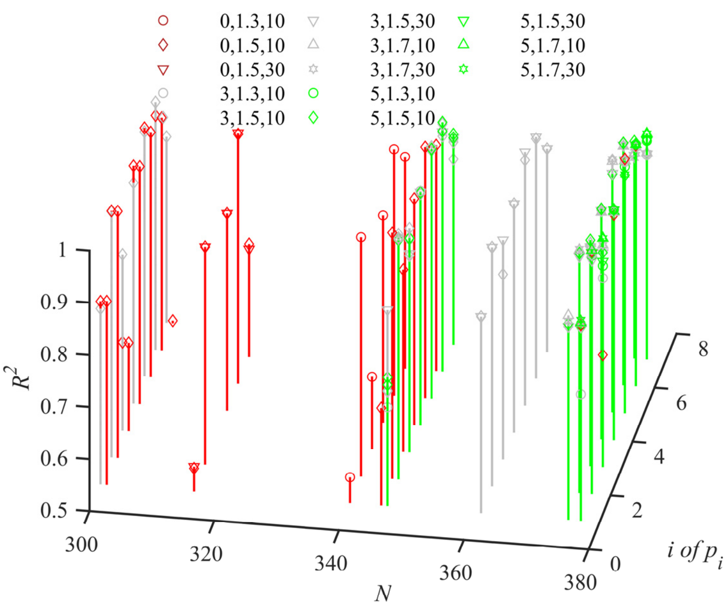

Figure 8. Surrogate models training with different sample points and combination of a_p, P_{min} and θ_{max}.

Table 2. Selected models for different performance.

p_i	R^2	MAE	N	a_p	θ_{max}	P_{min}
$\dot{m}_l$	0.886	0.011	377	5	30	1.7
$\dot{m}_h$	0.968	0.005	377	5	10	1.7
$\hat{\eta}$	0.938	0.001	377	5	30	1.7
$\hat{\pi}$	0.942	0.004	377	5	10	1.5
$\dot{m}_W$	0.987	0.003	377	0	10	1.5
π_W	0.965	0.001	377	5	10	1.5
η_W	0.920	0.005	377	5	30	1.5

2.2.3. Modified DDPG Algorithm

The DDPG algorithm [26] is a model-free and off-policy algorithm that can solve challenging problems robustly in a continuous state space, including high-dimensional problems. With the assistance of an actor–critic structure and replay buffer, the DDPG algorithm is appropriate for compressor design optimization. The Adam optimizer [38] and L2 normalization were applied, and the reward of the environment was defined by the performance metric $p_i \in \mathbb{P}$ of the rotors when implementing the algorithm.

It was observed that some distortion remained at the end of the MDP state sequences generated by trained agents, even with similar accumulated rewards. To decrease the distortion, the DDPG algorithm was modified in three aspects as follows. First, high-order feedback was applied to guide the exploration by recording the detected best state and delivering it to the environment. As a part of high-order feedback, randomness was added when resetting the environment. Second, an artificial tip was evaluated with an additional correction term δr_{art}, which improved the gradient near the detected optimized state and accelerated the training. Third, a virtual area extended the design space to ensure that the agent adequately explored the area near the boundary and the correction term δr_{vir} showed its effect.

$$r = a_1 r_{raw} + a_2 + \sum_{p_i \in \mathbb{P}} \delta r_{p_i} + \delta r_{art} + \delta r_{vir} \tag{4}$$

The reward of the environment was defined as expressed in Equation (4), where r_{raw} was a function of the performance p_i, which determined what the agents were expected to learn. In addition, a_1 and a_2 were constants used to scale r_{raw}. The punishment term δr_{p_i} indicated how much the performance p_i of a given state exceeded its reasonable range.

2.3. NSGA-II Application

NSGA-II [10] is a multiobjective evolutionary algorithm with nondominated sorting and crowding distance sorting. This algorithm has been widely used in compressor optimization problems.

2.3.1. NSGA-II Algorithm

Algorithm 1 showed the NSGA-II procedure, in which nondominated sorting, crowding distance sorting, and binary tournament selection were applied. The methods above lessen the computational complexity of NSGA-II relative to previous genetic algorithms. NSGA-II adapted to the multiobjective problems well and generated a Pareto front for these questions.

Algorithm 1: NSGA-II procedure [10]

```
Initialize a random parent population P_0
Create an offspring Q_0
for t = 0, N do
   Form the first combined population R_t = P_t ∪ Q_t
   Sort the R according to nondomination, and generate sets F_1, F_2, ..., F_l, ...
   Choose the best individuals F_l' in F_l using the crowded-comparison method
   Obtain the new population P_{t+1} = F_1 ∪ F_2 ∪ ... ∪ F_l'
   Create a new population Q_{t+1} by tournament selection, crossover and mutation
   t = t + 1
end for
Select individuals from the final population P_N
```

2.3.2. Fitness Function

Two fitness functions were established by the performances calculated in the RL environment with surrogate models. The genes of NSGA-II were the 18-dimensional design variable $s \in \mathbb{S}$, which is also the state of the RL environment. The two fitness functions expressed in Equation (5) aimed to improve the pressure ratio and efficiency.

$$\begin{aligned} f_1 &= \hat{\pi} - \hat{\pi}_0 - a_{1,1}N_{bad} - a_{1,2}\delta f_L - a_{1,2}\delta f_W \\ f_2 &= \hat{\eta} - \hat{\eta}_0 - a_{2,1}N_{bad} - a_{2,2}\delta f_L - a_{2,3}\delta f_W \end{aligned} \tag{5}$$

where f_1 and f_2 were the fitness functions and $\hat{\pi}_0$ and $\hat{\eta}_0$ were the reference values of the integrated pressure ratio $\hat{\pi}$ and integrated efficiency $\hat{\eta}$, respectively. N_{bad} was the number of dimensions of $p_i \in \mathbb{P}$ that were worse than the reference value p_i. The parameters $a_{i,j}$ ($i = 1, 2.$ $j = 1, 2, 3$) were constants indicating the strength of the correct terms.

$$\delta f_L = -\frac{1}{2}\|s - s_0\|_2^2 \tag{6}$$

The correction term δf_L provided L2 normalization of the design variables, as expressed in Equation (6), where s was the design variable and s_0 was the reference value. Normalization ensured that the design variable modifications would decay if they were located in dimensions that could not significantly influence the fitness function.

$$\delta f_W = a_W \left| \dot{m}_W - \dot{m}_{W,0} \right| \tag{7}$$

The correction term δf_W constrained the working point of the optimized rotors to change only minimally. As expressed in Equation (7), $\dot{m}_{W,0}$ was the working point of the reference rotor, and the constant a_W defined the strength and shape of δf_W. If $\dot{m}_W$ was modified excessively, δf_W increased and reduced the fitness functions.

2.4. The Combination of RL and GA

Since the agents learned the design policy in the whole design space, they can cooperate with the GA before the designers fully understand the mechanism of the policy. This universality was an intriguing aspect of intelligent design, and the cooperation showed advantages.

As shown in Figure 9, the GA process was considered the first step of the MDP, which provided information by giving the initiating state of the agents. In Figure 9a, the trained agents learned the design policy but could not determine the initial state to start an MDP itself, so the state of the reference rotor was selected as the initial state. After several modification steps, the performance improved, and the MDP ended. In Figure 9b, however, the result of the GA process acted as the initial state of the MDP. The agent gave different actions and made relatively minor modifications to the GA results, which kept the result gained by the GA when trying to improve the performance further.

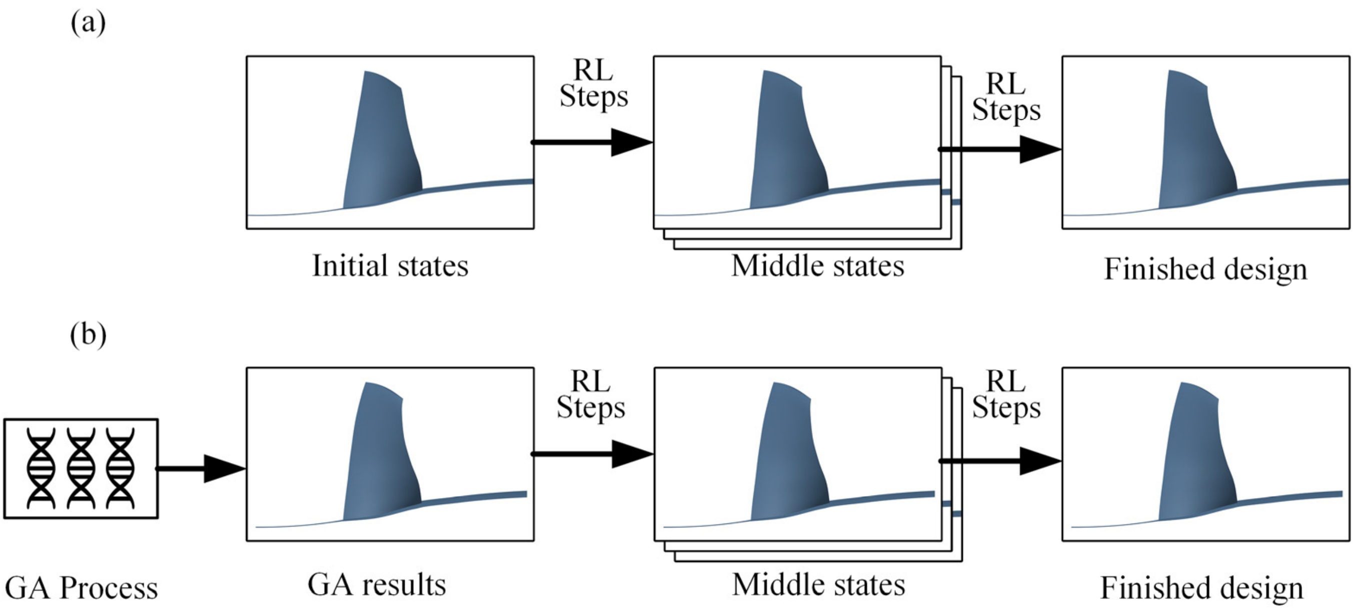

Figure 9. RL design process and its combination with GA: (**a**) RL process; (**b**) combination of RL and GA.

The combination merged the characteristics of RL and GA, where the two methods worked complementarily. The agents can learn and reuse different design policies, which avoids another GA process if the design objective changes. On the other hand, the GA result can be modified continuously to obtain the expected performance improvement.

3. Results

3.1. Policy for Improving the Pressure Ratios

The pressure ratio is one of the most noteworthy aspects of compressor performance. The stage pressure ratio improvement reduces the compressor's size and weight. In previous work, agents were trained to improve the pressure ratio of the rotors and successfully learned the design policy, with $r_{raw} = \hat{\pi} - \hat{\pi}_0$.

Figure 10 shows the operating characteristics of the rotors after different steps of modifications from the reference rotor. The more steps were taken, the higher the pressure ratio was. After the 15-step modification, $\dot{m}_W$ and η_W were almost equal to the reference, and π_W increased by 1.01%. The agent further improved the pressure ratio if a slight decrease in η_W was accepted. The trained agent could start the design at different states and modify the geometry very quickly, enabling cooperation with other optimization methods.

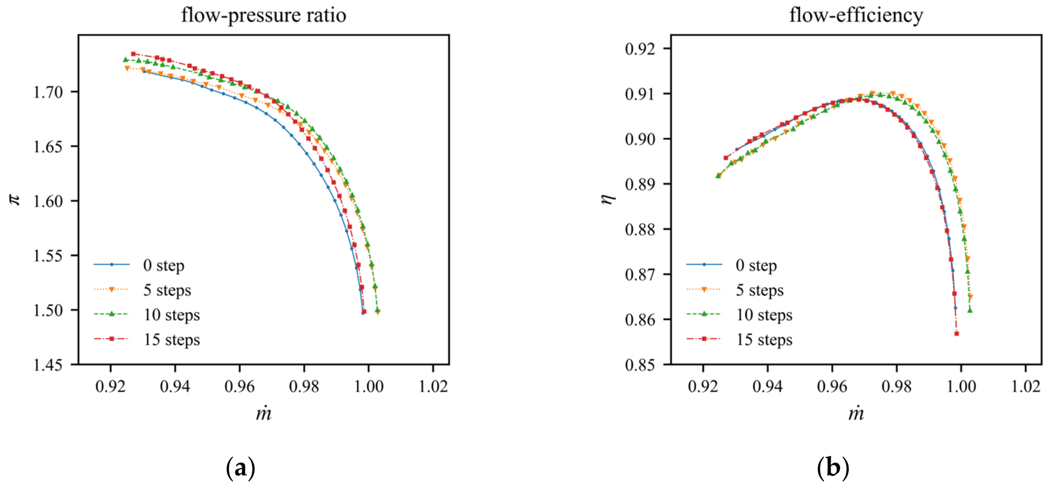

Figure 10. Operating characteristic variation in the rotors after different steps (from previous work). (**a**) Flow-pressure ratio. (**b**) Flow efficiency.

3.2. Optimization by NSGA-II

NSGA-II was applied to optimize the rotor to improve the pressure ratio and efficiency. The initial population P_0 was randomly generated in the normalized design space and then evolved by NSGA-II. The performance of individuals was evaluated using surrogate models in the RL environment.

The evolved population is shown in Figure 11, and the maximum fitness of each generation was monitored as shown in Figure 11a. As the evolution process continued and the calling times of surrogate models increased, the maximum fitness increased and fluctuated within a specific range. Surrogate models markedly reduced the calculation cost so that the population could evolve adequately. The population's fitness after 500 generations was plotted in Figure 11b, revealing a prominent Pareto front. The evolution of each condition was repeated five more times and plotted together, verifying that the influence of random parameters in the GA process had little influence on the results. The term δf_W changed the distribution of the fitness function, so the Pareto front was shorter than before, and its value changed after constraining the working point.

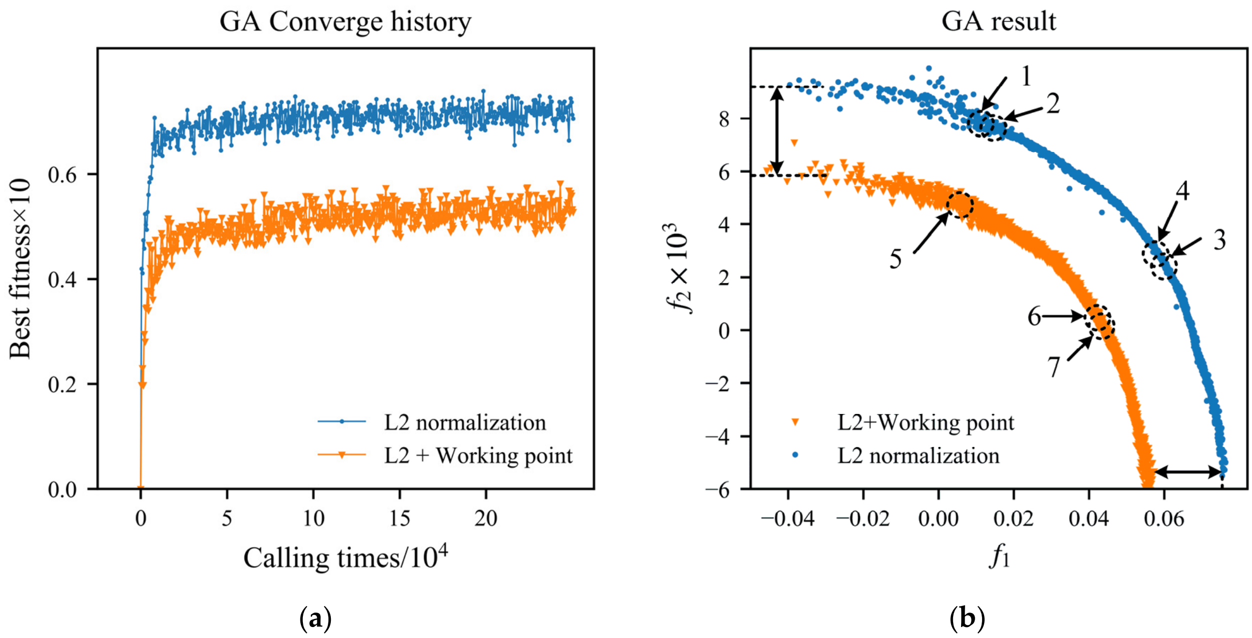

Figure 11. Evolution of the rotors using NSGA-II. (**a**) Convergence history. (**b**) Pareto front.

Seven individuals in the Pareto front were selected to check the operating characteristics, as also marked in Figure 11b, from which the individuals with specific fitness and minimum geometry modification were selected. For the L2 normalized condition, the ranges were $f_1 \in [0.05,\ 0.07]$ and $f_1 \in [0,\ 0.01]$, while for the L2 normalized + working point condition, the ranges were $f_1 \in [0.04,\ 0.05]$ and $f_1 \in [0,\ 0.01]$.

Figure 12 shows that the operating characteristics, pressure ratio and efficiency of the selected individuals improved. The efficiency of cases 1 and 2 improved more, and their pressure ratio improved less, while cases 3 and 4 gained a greater pressure ratio improvement, meeting the predictions of the fitness functions. Therefore, the NSGA-II algorithm worked well with the assistance of surrogate models, and the results were physically verifiable.

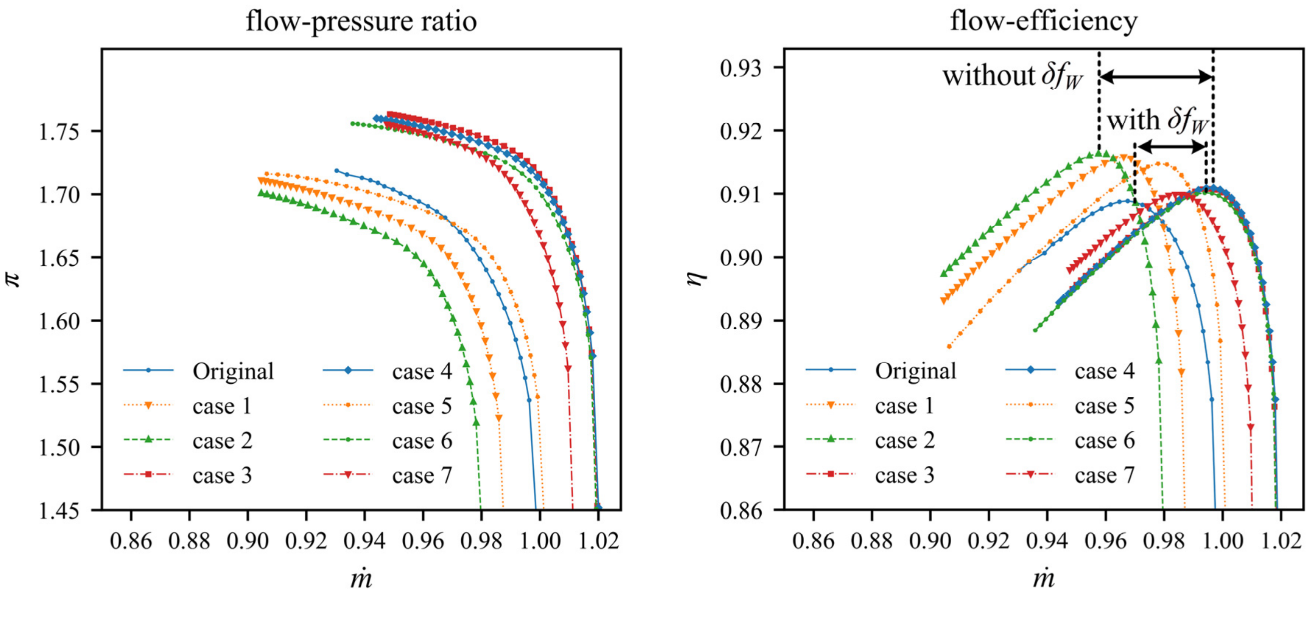

(**a**) (**b**)

Figure 12. Operating characteristics of selected individuals. (**a**) Flow-pressure ratio. (**b**) Flow efficiency.

The average mass flow variation at the working point of the final population $d\overline{m}_W$ was calculated as $d\overline{m}_W$ = 0.0016 before applying the working point constraint and decreased by 61.25% to 0.0069 after δf_W was added. As also shown in Figure 12b, the working points of cases 5, 6, and 7 were closer to the original case and to each other, showing that δf_W worked well.

GA optimization can be considered one step in the design process and integrated into the RL framework. The design variables can be modified directly and continuously using the trained agent to match the expected performance. For the GA, the Pareto front has no straightforward relations to other points in the design space. The nearby points in the Pareto front can have entirely different design variables. Therefore, another evolution process was necessarily performed to generate modification steps similar to those of the agents. In addition, prior knowledge was still required to define the fitness function and select individuals using GA optimization.

3.3. Cooperation of the RL Agents and GA

The GA process was integrated into the RL framework as one kind of MDP step. Case 1, as shown in Figure 12, obtained a significant efficiency improvement, but the pressure ratio was lower than that of the reference. The agent trained as described in Section 3.1 provided a way to directly improve the pressure ratio by directly modifying the design variables of the case 1 rotor.

Figure 13 showed the operation characteristics of the modified rotors, in which the pressure ratio increased incrementally, and the efficiency declined slightly. After 12 steps, the rotor gained a pressure ratio equal to the reference for almost all mass flows, and a higher efficiency was also maintained. The chock mass flow rate of the GA case 1 rotor was less than the reference, and the agent also improved the chock mass flow rate of the modified agents.

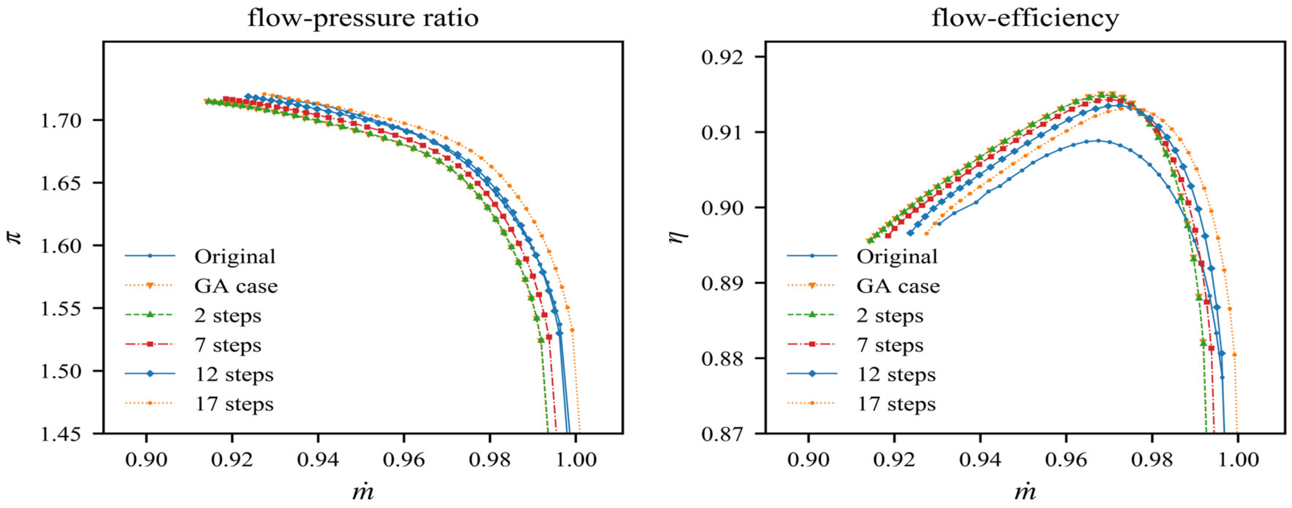

(**a**) (**b**)

Figure 13. Operation characteristics of the modified rotors. (**a**) Flow-pressure ratio. (**b**) Flow efficiency.

The variations in the near-peak efficiency performance metrics π_W and η_W were plotted in Figure 14. The performance of different rotors at the same mass flow rate $\dot{m}_{W,0}$ was also considered, where $\dot{m}_{W,0}$ was the peak efficiency mass flow rate of the reference rotor. The parameters $\pi_{W,0}$ and $\eta_{W,0}$ denoted the pressure ratio and efficiency of the reference rotor at $\dot{m}_{W,0}$, respectively. The pressure ratio at $\dot{m}_{W,0}$ raised by approximately 0.52% from the GA case 1 result. The efficiency at $\dot{m}_{W,0}$ became higher than $\pi_{W,0}$ after modification by the agent, and the π at near-peak efficiency also improved. The pressure ratio was found to be further increased when agent modification was conducted over additional steps.

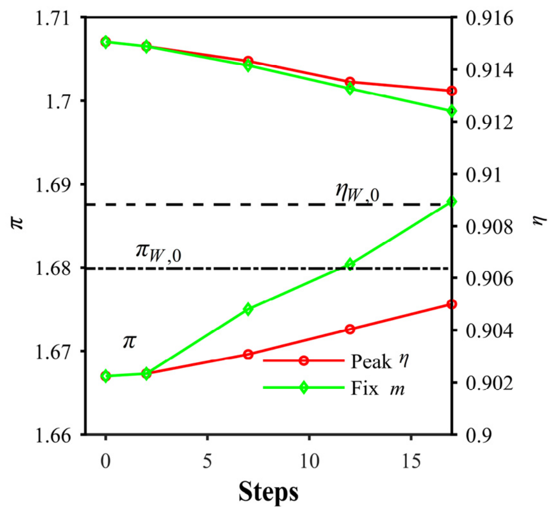

Figure 14. Performance variation during modification.

The variations in the geometric parameters m, θ, χ_{in}, χ_{out}, and β_y through the spanwise direction were shown in Figure 15. A combined sweep feature was introduced in GA case 1, and the rotor swept forward over most of the span and swept back at the tip region. The agent reduced the amplitude of the sweep feature in both forward and backward directions. Case 1 also acquired a blade lean feature with negative $d\theta$, and the agent diminished this feature. The agent also changed χ_{in} and χ_{out}, so the airfoil segment angle $\Delta\beta$ rose at the tip and decreased at the hub relative to the GA case. The parameter β_y improved at all spans in case 1 and was diminished by the agent, especially at the tip and hub. Rotors were also plotted in $Z - R$ and $Z - \theta r$ surfaces as shown in Figure 16, where the parameter variations showed its effect on the rotor geometries.

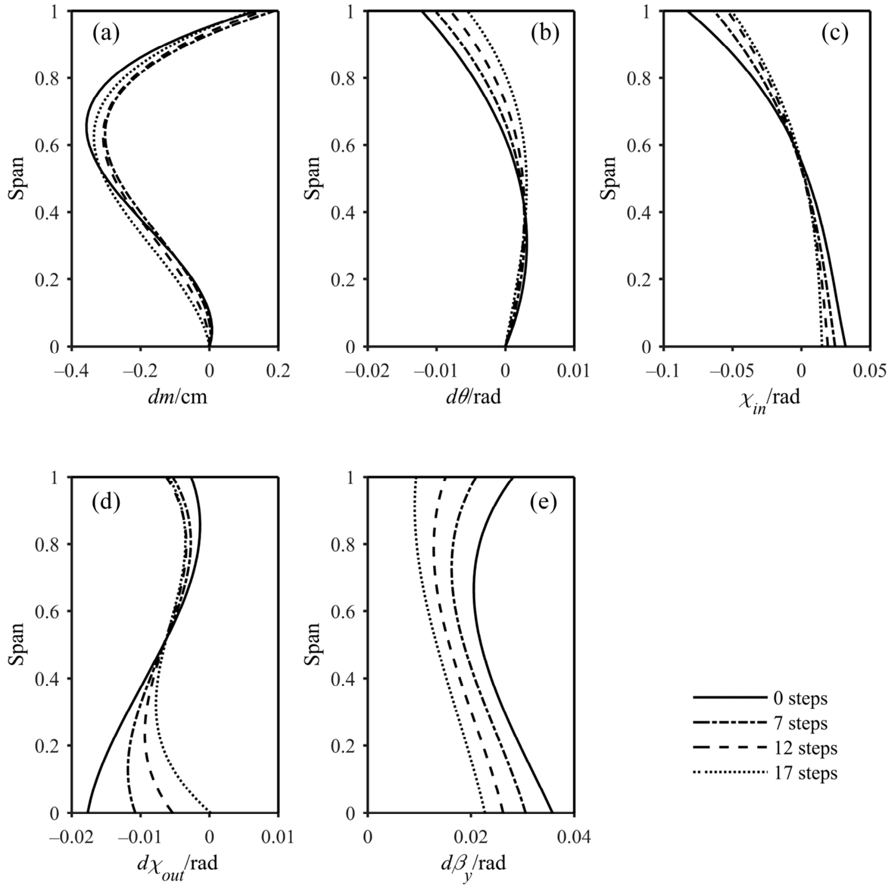

Figure 15. Geometry variation distribution of the span after cooperation: (**a**) meridional coordinate, (**b**) tangential direction, (**c**) inlet camber angle, (**d**) outlet camber angle, and (**e**) incidence angle.

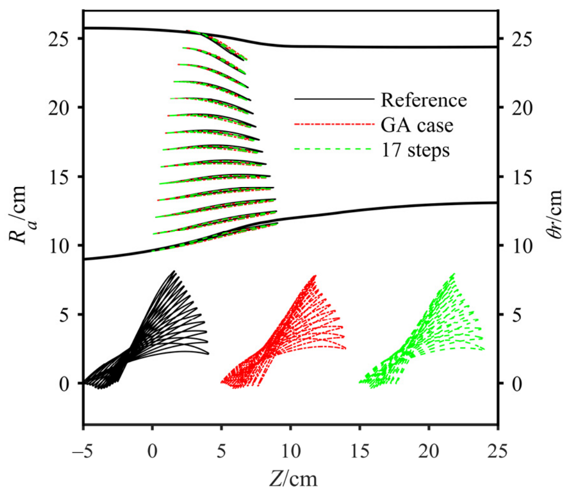

Figure 16. Rotors in $Z - R$ and $Z - \theta r$ surface.

4. Discussion

4.1. Performance Distribution

The GA process generated a modified rotor case 1 with a much higher efficiency and slightly lower pressure ratio, and the agent modified the GA result to further improve the pressure ratio. Different design variables changed and influenced the flow simultaneously, making it relatively complex to interpret. The flow mechanisms were analyzed, showing that geometric modifications were effective and considerably interpretable.

The deviation of the local pressure ratio π, the local efficiency η, and the absolute flow angle $\Delta\alpha$ were plotted in Figure 17. The local η at the near tip region increased and $\Delta\alpha$ decreased in the GA case, which was noted as 0 steps, so the total η improved. The local π diminished at all spanwise locations, especially those higher than 50%, resulting in a decline in the total π.

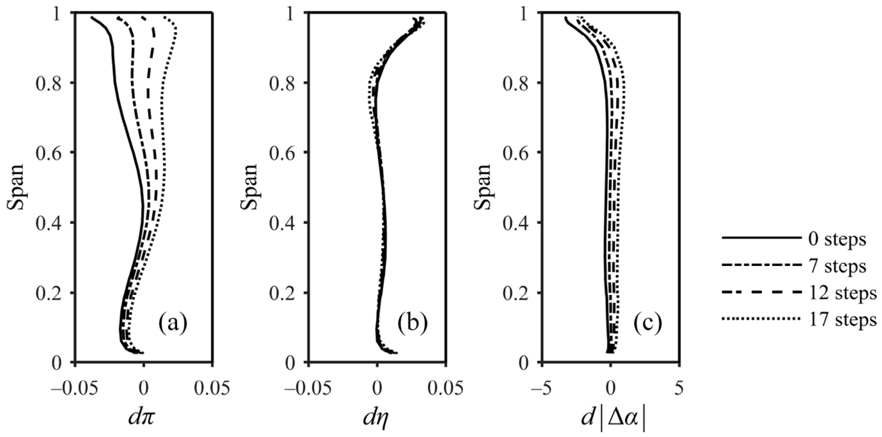

Figure 17. Deviation of the local performance distribution in different spans: (**a**) pressure ratio, (**b**) efficiency, and (**c**) absolute flow angle.

Then, as the geometry was incrementally modified by the agent, the local pressure ratio π increased. The local π at spanwise locations higher than 50% surpassed the reference after 17 steps, which contributed most of the π improvement. The local π near the hub was also decreased in GA case 1 and improved by the RL agent, with a smaller variation range than the tip section. Together with π, $\Delta\alpha$ increased spanwise by the RL agent, mainly because of the variation in the design variables β_y, χ_{in}, and χ_{out}. The agent maintained most of the η improvement gained by the GA while slightly decreasing the local η at 80% spanwise of the rotor after modification.

4.2. Flow Field Details

The flow field details of the reference rotor, GA case rotor and the result rotors after modification by the agent were analyzed and compared in this section, indicating that the improvements were convictive and explicable. The combination of sweep, lean, and change in other design variables contributed to the improvements.

The forward sweep of rotor blades can improve the efficiency and the stable operating range, according to Zhen et al. [39]. The sweep feature changed the shape of the passage shock, so the shock loss and pressure ratio of GA case 1 were reduced. Denton [40] affirmed that the shock waves in the tip region of the transonic rotor are essential for the pressure ratio, so the local pressure ratio of the GA case decreased at the tip region. The agent improved χ_{in}, reduced χ_{out}, and simultaneously changed β_y to increase the pressure ratio.

Figure 18 shows the isentropic Mach number distribution at 70% and 90% spans. The GA step decreased the isentropic Mach number of the suction surface, showing that the shock wave was weakened. Then, the RL agent moved the peak isentropic Mach number location toward the leading edge, with the value remaining unchanged. At the pressure surface, the isentropic Mach number near the leading edge declined upon the GA process and reduced even further upon the agent's modification.

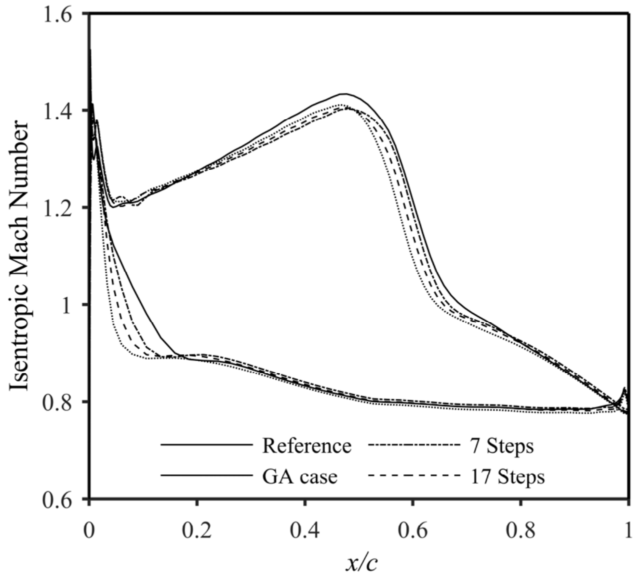

(**a**)

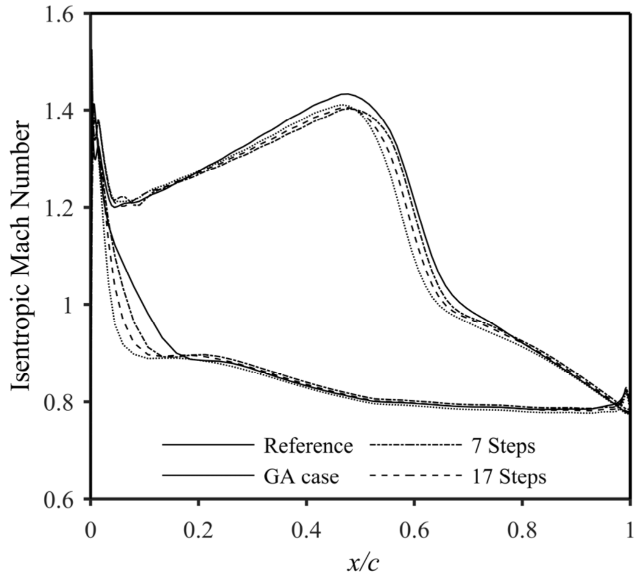

(**b**)

Figure 18. Isentropic Mach number distribution through the chord line at spans of 70% and 90%: (**a**) 70% span; (**b**) 90% span.

The pressure gradient perpendicular to the end wall must be zero, according to the illustration of Denton and Xu [41]. Therefore, back sweep at the tip region would reduce the load of the rotor near the trailing. The relative Mach number of the reference rotor, GA case 1, and the rotor after 17 steps of modification of agents was plotted in Figure 19 to visualize the separation region of the rotors. The load reduction and the airfoil segment angle change downsized the separation near the tip, which is one of the reasons why the local η increased. Then, the separation did not increase after agent modification, which helped maintain efficiency.

As marked in the 90% span surface, the shock wave at the leading edge and in the passage could be identified. The forward sweep feature diminished the Mach number before the shock waves compared to the reference, as shown in Figure 19b, which reduced the shock loss and the pressure rise. After modification by RL agents in Figure 19c, the shock wave at the leading edge became stronger and consequently increased the pressure ratio, while the passage shock wave remained nearly unchanged. In addition, since the shock waves changed, the peak relative Mach number at 50% and 70% span also lowered slightly.

A combined lean feature was also introduced and modified. According to Sasaki and Breugelmans [42], a lean feature caused unloading near the end wall and overloading around the mid-span if the angle between the end wall and the suction surface was obtuse. Shang et al. [43] explained that lean features work because they generate a pressure gradient and drive low-energy flow through the radial direction.

Figure 20 showed the radial velocity Vr distribution at the 80% length axial surface to analyze the radial secondary flow. The air near the suction surface flowed from the hub to the shroud because of the centrifugal force and was influenced by the radial pressure surface. The maximum Vr near the suction surface and the minimum Vr at the same spanwise location were plotted for each rotor, and it was apparent that Vr declined after introducing the lean feature. As the RL agent modified the rotor further, Vr increased slightly because the lean feature was slightly diminished.

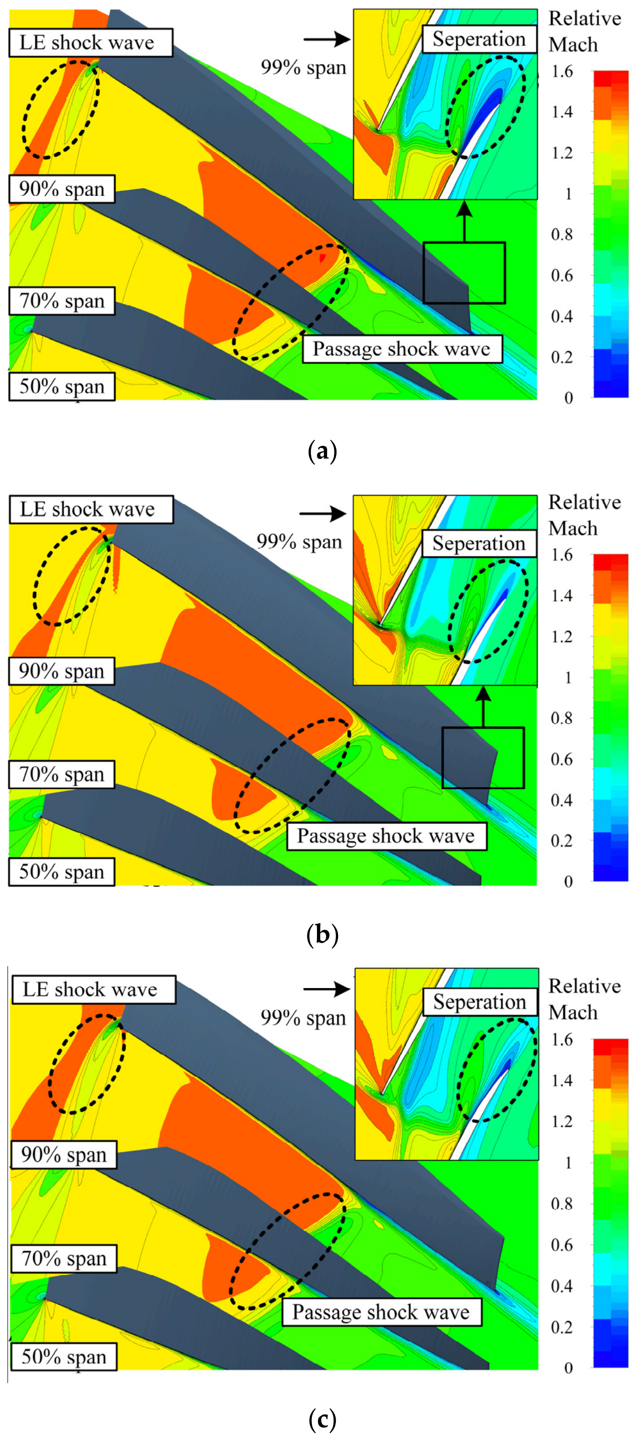

Figure 19. Relative Mach number distribution of the different rotors. (**a**) Distribution of the reference rotor. (**b**) Distribution of the GA case. (**c**) Distribution after modification by the agent.

A tip leakage vortex (TLV) was generated by the pressure difference between the pressure surface and suction surface and interacted with the shock waves, which influenced the performance of the rotors. The geometric modifications changed the pressure distribution and affected the TLV.

The strength of the TLV depends on the chordwise integration of the pressure difference between the pressure surface and the suction surface, as illustrated by Chima [44]. Therefore, even though the TLV was stronger when it was just initiated because of the higher pressure difference near the leading edge, it was weakened after development because of the lower pressure of difference at the rear spanwise.

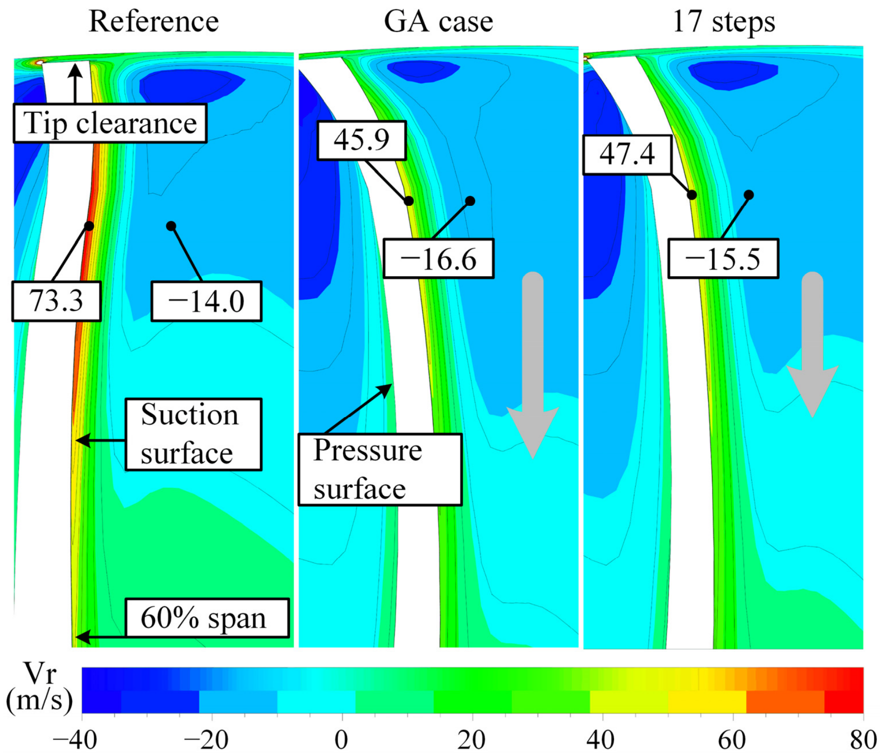

Figure 20. Radial velocity at the axial surface (80% length).

Figure 21 showed the static pressure distribution around the blade, at the near tip spanwise at 90% and around the tip clearance spanwise at 99.8%. The tip of the rotor was swept back, so the load was larger after the GA step, but χ_{in} near the tip decreased, so the peak static pressure at the pressure surface in Figure 21a did not increase much, and the location moved. Then, when the agent introduced more back sweeps and rose χ_{in}, the peak static pressure increased and moved farther toward the leading edge. The minimum static pressure near the tip and around the tip clearance was increased, and the modification of the agent further improved the static pressure downstream after the minimum location.

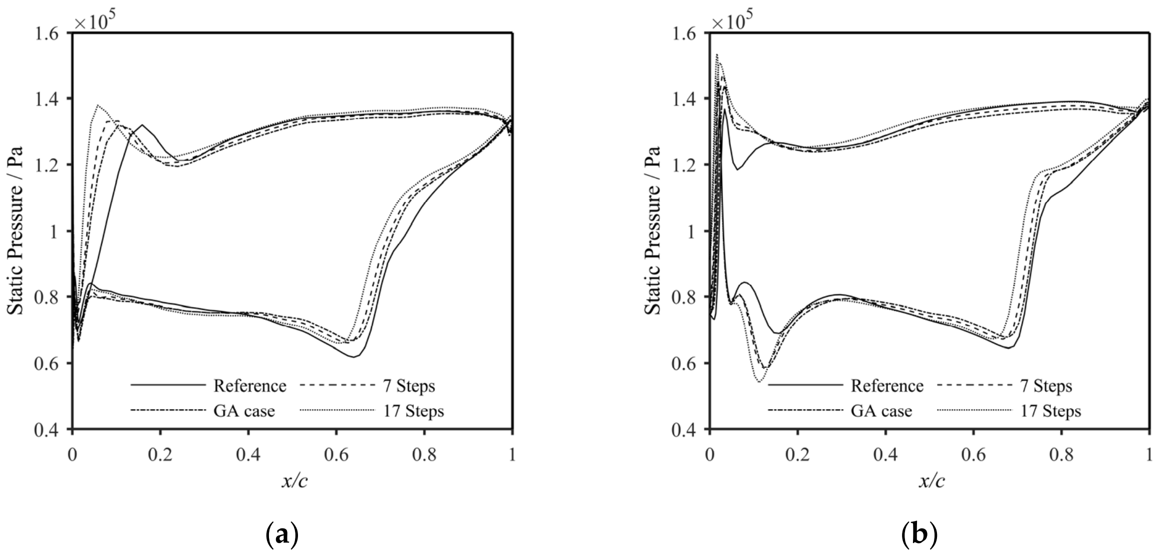

Figure 21. Static pressure distribution through the chord line near and around the tip span: (**a**) 90% span; (**b**) 99.8% span.

Figure 22 showed the tip clearance flow feature of the rotors, together with the static pressure distribution at a 98% span. It was observed that the TLV did not expand after modification, even when the pressure difference between the pressure surface and suction surface increased near the leading edge.

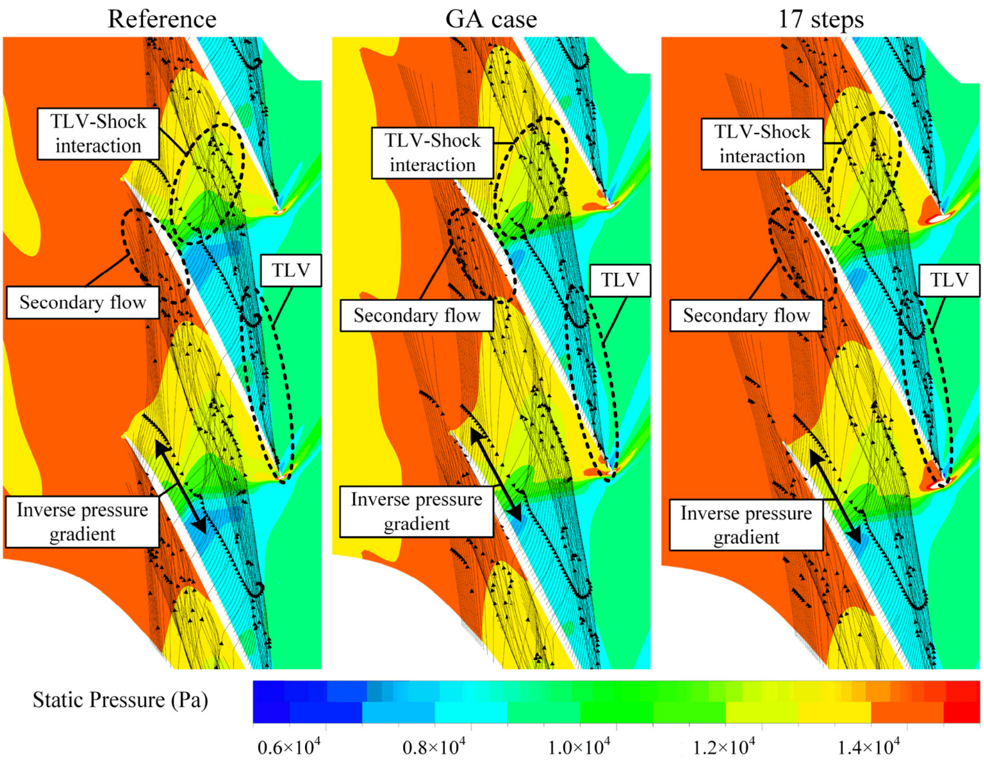

Figure 22. Tip leakage flow of the rotors and static pressure distribution at 99.8% spanwise.

The passage shock wave caused a severe rise in pressure, which can interact with the TLV and distort it, as analyzed by Suder [45]. The inverse pressure gradient declined in the GA case and the RL results, as plotted in Figure 22. As a result, the distortion of the TLV was diminished compared with the reference rotor case, which helped raise the overall efficiency.

The modifications added by GA and RL also enhanced the flow field by influencing the end wall secondary flow. As emphasized in Figure 22, the leakage flow in the reference rotor moved across the whole passage and passed the next tip clearance, which generated considerable loss. In the flow field of the GA case, a larger portion of the leakage flow was directed downstream rather than toward the next tip clearance. This flow feature remained after the RL agents modified the rotor and benefited the overall efficiency.

The static pressure downstream in Figure 22 indicated the change in the pressure ratio, which also agreed with the local pressure ratio change in Figure 17. The flow with relatively high static pressure mixed with the flow at lower spanwise, and the static pressure decreased. The static pressure downstream was lower than the reference; then, upon modification by the RL agent, the static pressure improved and became higher than the reference.

Figure 23 showed the entropy distribution at the outlet of the rotors in the axial surface, which also indicated the improvement after the modifications. As marked by arrows, the thickness of the flow area with relatively high entropy decreased in the GA case, then slightly increased in the RL result and remained better than the reference. A similar reduction in entropy appeared in the wake flow area, as marked in the dashed circle, where the high entropy area was reduced.

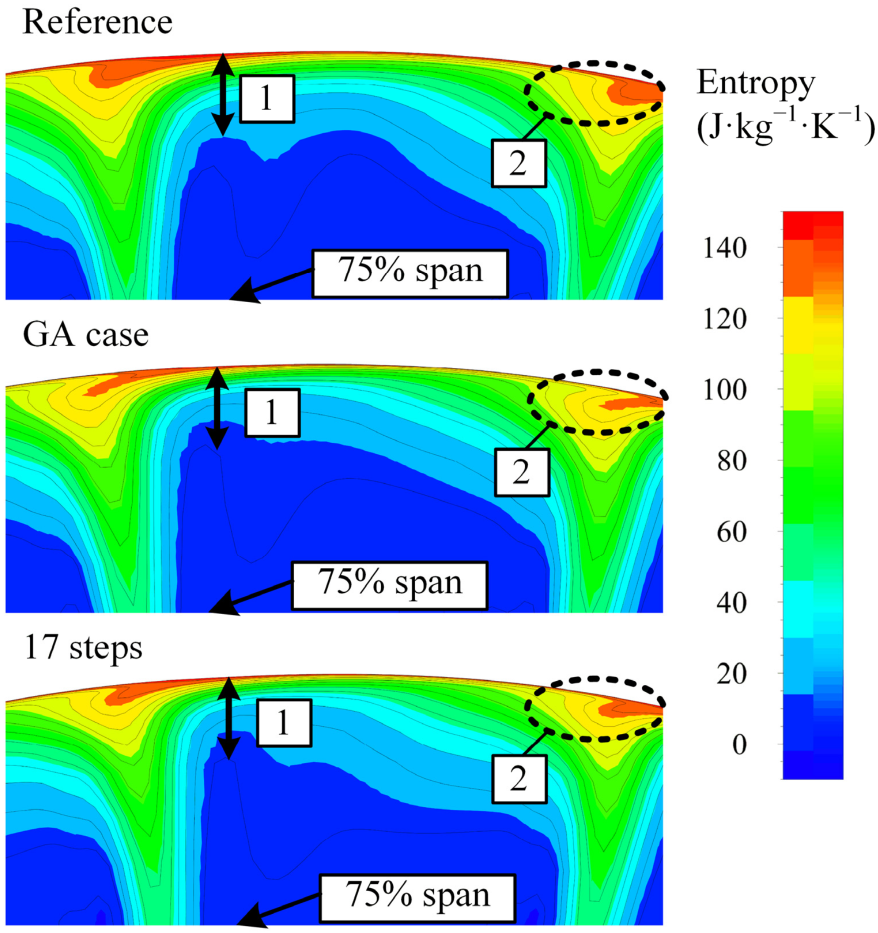

Figure 23. Entropy distribution of the meridional velocity at 50% and 80% of the axial length.

In summary, the GA step improved the efficiency by adding a combined sweep feature and a combined lean feature and changing the 2D airfoil features. The efficiency improvement arose mainly from the separation and shock wave reduction, which simultaneously declined the pressure ratio. Then, the agent modified the 3D feature, changed the distribution of χ_{in}, χ_{out}, and decreased β_y to obtain a higher pressure ratio. Most of the beneficial features of the flow field were retained, so the efficiency remained high compared with that of the reference rotor.

4.3. Computational Cost

The computational cost has always been a primary concern in compressor design optimization. The computation consumption of the RL agent and GA process was considered in this section. Since the surrogate models accounted for most of the computational cost, it was appropriate to evaluate different algorithms' costs in training and execution by counting the calling time of surrogate models.

The convergence history when training the agent was plotted in Figure 24, where the mean line was calculated by all R curves still in training. The training process was repeated several times to reduce the influence of randomness in network initialization and noise action. The mean R increased before 5000 episodes, and many agents converged and stopped training, so the mean R decreased at 5000–6000 episodes. One episode contained 100 steps, so 5000 episodes corresponded to 500,000 calls of the surrogate model, approximately two times that of the NSGA-II evolutionary process and on the same order of magnitude. The agent learned the policy of the whole design process with the same order of magnitude of computational cost as NSGA-II learning a Pareto front.

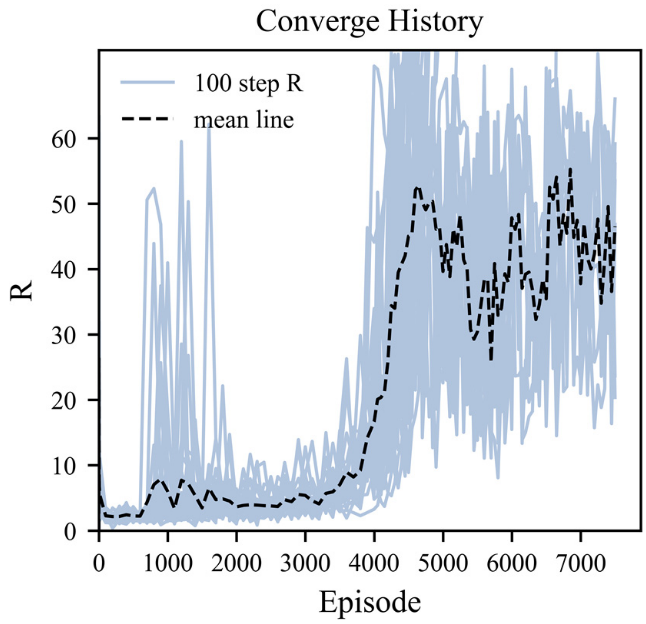

Figure 24. Convergence history of the agent.

The trained agent showed its advantage in generating the new design because of the different running logic. Agents could modify all designs in the design space and improve the performance designers expect, with only one calling surrogate model for each step. The modified design variables changed continuously.

For the GA, the Pareto front had no straightforward relations to other points in the design space. The nearby points in the Pareto front could have entirely different design variables. Therefore, another evolution process needed to be performed with different fitness functions and extra constraints to generate modification steps similar to those of the agents. Thus, the agents yielded modifications much faster than the GA. As described in Section 3.2, one GA step consumed 14,705 times the calling times of surrogate models as 17 RL steps.

In summary, training agents had a higher computational cost than the GA, but the trained agents produced modifications much faster. It was appropriate to initialize the RL design process at the GA results rather than initiate at the reference or random design states and then modify the rotor using trained agents to obtain rotors that met the requirements.

5. Conclusions

This study showed that the modified DDPG and NSGA-II algorithms could work in conjunction in the RL framework, combining the universality of RL agents and the effectiveness of the GA process and demonstrating the corresponding advantages. The trained agent modified one of the GA result cases, improved the pressure ratio from lower than the reference to higher than the reference, and maintained high efficiency.

The new rotor obtained a sweep and lean feature, and the associated 2D airfoils were modified. The flow field analysis evidence suggested that the modifications made by the agent and GA process were explicable. It was revealed that the efficiency of the redesigned rotor improved because the separation near the tip was released, the shock wave weakened, the influence of the TLV was reduced, and the radial secondary flow was alleviated. These beneficial features remained after agent modification, and the pressure ratio improved mainly because of the increase in the flow turn angle.

The agents with the modified DDPG algorithm learned a valid policy to improve the pressure ratio across the whole design space. The results of the NSGA-II algorithm indicated that novel fitness functions reduced the variation in geometry modification and working points. The integration of the trained agent and GA process yielded favorable results with a higher pressure ratio and efficiency. Moreover, the computational costs were compared, showing that agents modified the design much faster than the GA process, with more training of agents cost.

The results of this study indicated that the RL method could incorporate other methods and that better designs could be generated by combining agents with different policies, GA methods, prior knowledge, and other optimization methods. More efforts are needed to improve the RL methods and surrogate models, involving, for example, hierarchical RL to extend the generalization ability. The RL methods can be further applied to assist future compressor design and have the potential to complete the design automatically and utilize more existing knowledge after improvement.

Author Contributions: Conceptualization, X.X.; methodology, X.X.; software, X.X.; validation, X.X.; formal analysis, X.X. and D.B.; investigation, X.X.; resources, X.H. and M.Z.; data curation, X.X.; writing—original draft preparation, X.X. and D.B.; writing—review and editing, X.X., D.B. and X.H; visualization, X.X. and D.B.; supervision, M.Z.; project administration, X.H.; funding acquisition, M.Z. All authors have read and agreed to the published version of the manuscript.

Funding: This research received no external funding.

Institutional Review Board Statement: Not applicable.

Informed Consent Statement: Not applicable.

Data Availability Statement: The data presented in this study are available on request from the corresponding author.

Conflicts of Interest: The authors declare no conflict of interest.

References

1. Biollo, R.; Ernesto, B. Recent advances in transonic axial compressor aerodynamics. *Prog. Aerosp. Sci.* **2013**, *56*, 1–18. [CrossRef]
2. Smith, L.H. Axial Compressor Aerodesign Evolution at General Electric. *J. Turbomach.* **2002**, *124*, 321–330. [CrossRef]
3. Horlock, J.H.; Denton, J.D. A Review of Some Early Design Practice Using Computational Fluid Dynamics and a Current Perspective. *J. Turbomach.* **2005**, *127*, 5–13. [CrossRef]
4. Pinto, R.N.; Afzal, A.; D'Souza, L.V.; Ansari, Z.; Samee, A.D.M. Computational Fluid Dynamics in Turbomachinery: A Review of State of the Art. *Arch. Comput. Methods Eng.* **2016**, *24*, 467–479. [CrossRef]
5. Dunham, J. *CFD Validation for Propulsion System Components*; AGARD Advisory Report 355; AGARD: Quebec, QC, Canada, 1998.
6. Kim, K.-Y.; Samad, A.; Benini, E. *Design Optimization of Fluid Machinery: Applying Computational Fluid Dynamics and Numerical Optimization*; John Wiley & Sons, Incorporated: Newark, NJ, USA, 2019.
7. Li, Z.; Zheng, X. Review of design optimization methods for turbomachinery aerodynamics. *Prog. Aerosp. Sci.* **2017**, *93*, 1–23. [CrossRef]
8. Benini, E. Three-Dimensional Multi-Objective Design Optimization of a Transonic Compressor Rotor. *J. Propuls. Power* **2004**, *20*, 559–565. [CrossRef]
9. Bonaiuti, D.; Zangeneh, M. On the Coupling of Inverse Design and Optimization Techniques for the Multiobjective, Multipoint Design of Turbomachinery Blades. *J. Turbomach.* **2009**, *131*, 021014. [CrossRef]
10. Deb, K.; Pratap, A.; Agarwal, S.; Meyarivan, T. A fast and elitist multiobjective genetic algorithm: NSGA-II. *IEEE Trans. Evol. Comput.* **2002**, *6*, 182–197. [CrossRef]
11. Samad, A. *Turbomachinery Design*; LAP LAMBERT Academic Publishing GmbH & Co. KG: Saarbrucken, Germany, 2012.
12. Wang, X.D.; Hirsch, C.; Kang, S.; Lacor, C. Multi-objective optimization of turbomachinery using improved NSGA-II and approximation model. *Comput. Methods Appl. Mech. Eng.* **2011**, *200*, 883–895. [CrossRef]
13. Ma, S.-B.; Roh, M.-S.; Kim, K.-Y. Optimization of Discrete Cavities with Guide Vanes in A Centrifugal Compressor based on a Comparative Analysis of Optimization Techniques. *Int. J. Aeronaut. Space Sci.* **2021**, *22*, 514–530. [CrossRef]
14. Eberhart, R.; Kennedy, J. A new optimizer using particle swarm theory. In Proceedings of the Sixth International Symposium on Micro Machine and Human Science (MHS'95), Nagoya, Japan, 4–6 October 1995; pp. 39–43.
15. Tang, X.; Luo, J.; Liu, F. Aerodynamic shape optimization of a transonic fan by an adjoint-response surface method. *Aerosp. Sci. Technol.* **2017**, *68*, 26–36. [CrossRef]
16. Du, Q.W.; Yang, L.K.; Li, L.L.; Liu, T.Y.; Zhang, D.; Xie, Y.H. Aerodynamic design and optimization of blade end wall profile of turbomachinery based on series convolutional neural network. *Energy* **2022**, *244*, 122617. [CrossRef]
17. Sutton, R.S.; Barto, A.G. *Reinforcement Learning: An Introduction*, 2nd ed.; The MIT Press: Cambridge, MA, USA; London, UK, 2020.
18. Tan, R.K.; Liu, Y.; Xie, L. Reinforcement learning for systems pharmacology-oriented and personalized drug design. *Expert Opin. Drug Discov.* **2022**, *17*, 849–863. [CrossRef] [PubMed]

19. Senior, A.W.; Evans, R.; Jumper, J.; Kirkpatrick, J.; Sifre, L.; Green, T.; Qin, C.; Zidek, A.; Nelson, A.W.R.; Bridgland, A.; et al. Improved protein structure prediction using potentials from deep learning. *Nature* **2020**, *577*, 706–710. [CrossRef] [PubMed]
20. Fawzi, A.; Balog, M.; Huang, A.; Hubert, T.; Romera-Paredes, B.; Barekatain, M.; Novikov, A.; Ruiz, F.J.R.; Schrittwieser, J.; Swirszcz, G.; et al. Discovering faster matrix multiplication algorithms with reinforcement learning. *Nature* **2022**, *610*, 47–53. [CrossRef]
21. Sigaud, O.; Stulp, F. Policy search in continuous action domains: An overview. *Neural Netw.* **2019**, *113*, 28–40. [CrossRef]
22. Viquerat, J.; Rabault, J.; Kuhnle, A.; Ghraieb, H.; Larcher, A.; Hachem, E. Direct shape optimization through deep reinforcement learning. *J. Comput. Phys.* **2021**, *428*, 110080. [CrossRef]
23. Schulman, J.; Wolski, F.; Dhariwal, P.; Radford, A.; Klimov, O. Proximal Policy Optimization Algorithms. *Comput. Res. Repos.* **2017**, arXiv:1707.06347. [CrossRef]
24. Li, R.; Zhang, Y.; Chen, H. Learning the Aerodynamic Design of Supercritical Airfoils through Deep Reinforcement Learning. *AIAA J.* **2021**, *59*, 3988–4001. [CrossRef]
25. Qin, S.; Wang, S.; Wang, L.; Wang, C.; Sun, G.; Zhong, Y. Multi-Objective Optimization of Cascade Blade Profile Based on Reinforcement Learning. *Appl. Sci.* **2020**, *11*, 106. [CrossRef]
26. Lillicrap, T.P.; Jonathan, J.H.; Pritzel, A.; Heess, N.; Erez, T.; Tassa, Y.; Silver, D.; Wierstra, D. Continuous control with deep reinforcement learning. *Comput. Sci.* **2019**, arXiv:1509.02971. [CrossRef]
27. Li, J.; Zhang, M.; Martins, J.R.R.A.; Shu, C. Efficient Aerodynamic Shape Optimization with Deep-Learning-Based Geometric Filtering. *AIAA J.* **2020**, *58*, 4243–4259. [CrossRef]
28. Hammond, J.; Pepper, N.; Montomoli, F.; Michelassi, V. Machine Learning Methods in CFD for Turbomachinery: A Review. *Int. J. Turbomach. Propuls. Power* **2022**, *7*, 16. [CrossRef]
29. Hammond, J.; Montomoli, F.; Pietropaoli, M.; Sandberg, R.D.; Michelassi, V. Machine Learning for the Development of Data-Driven Turbulence Closures in Coolant Systems. *J. Turbomach.* **2022**, *144*, 081003. [CrossRef]
30. Wang, Z.Y.; Qu, F.; Wang, Y.H.; Luan, Y.G.; Wang, M. Research on the lean and swept optimization of a single stage axial compressor. *Eng. Appl. Comput. Fluid Mech.* **2021**, *15*, 142–163. [CrossRef]
31. Duan, Y.; Zheng, Q.; Jiang, B.; Lin, A.; Zhao, W. Implementation of Three-Dimensional Inverse Design and Its Application to Improve the Compressor Performance. *Energies* **2020**, *13*, 5378. [CrossRef]
32. Ren, X.; Gu, C. Investigation of Compressor Tip Clearance Flow Based on the Discontinuous Galerkin Methods. In Proceedings of the ASME Turbo Expo 2013: Turbine Technical Conference and Exposition, San Antonio, TX, USA, 3–7 June 2013. [CrossRef]
33. Strazisar, A.J.; Wood, J.R.; Hathaway, M.D.; Suder, K.L. *Laser Anemometer Measurements in a Transonic Axial-Flow Fan Rotor*; NASA-TP-2879; NASA: Cleveland, OH, USA, 1989.
34. Jung, Y.-J.; Jeon, H.; Jung, Y.; Lee, K.-J.; Choi, M. Effects of recessed blade tips on stall margin in a transonic axial compressor. *Aerosp. Sci. Technol.* **2016**, *54*, 41–48. [CrossRef]
35. Chen, H.; Huang, X.; Fu, S. CFD Investigation on Stall Mechanisms and Casing Treatment of a Transonic Compressor. In Proceedings of the 42nd AIAA/ASME/SAE/ASEE Joint Propulsion Conference, Sacramento, CA, USA, 9–12 July 2006.
36. Forrester, A.I.J. *Engineering Design via Surrogate Modelling: A Practical Guide*; Wiley: Chichester, UK, 2008.
37. Morris, M.D.; Mitchell, T.J. Exploratory designs for computational experiments. *J. Stat. Plan. Inference* **1995**, *43*, 381–402. [CrossRef]
38. Kingma, D.P.; Ba, J. Adam: A Method for Stochastic Optimization. *CoRR* **2015**, arXiv:1412.6980. [CrossRef]
39. Zheng, X.; Li, Z. Blade-end treatment to improve the performance of axial compressors: An overview. *Prog. Aerosp. Sci.* **2017**, *88*, 1–14. [CrossRef]
40. Denton, J.D. The Effects of Lean And Sweep on Transonic Fan Performance: A Computational Study. *TASK Q.* **2002**, *6*, 7–23.
41. Denton, J.D.; Xu, L. The exploitation of three-dimensional flow in turbomachinery design. *Proc. Inst. Mech. Eng. Part C J. Mech. Eng. Sci.* **1998**, *213*, 125–137. [CrossRef]
42. Sasaki, T.; Breugelmans, F. Comparison of Sweep and Dihedral Effects on Compressor Cascade Performance. *J. Turbomach.* **1998**, *120*, 454–463. [CrossRef]
43. Shang, E.; Wang, Z.Q.; Su, J.X. The Experimental Investigations on the Compressor Cascades with Leaned and Curved Blade. In Proceedings of the ASME 1993 International Gas Turbine and Aeroengine Congress and Exposition, Cincinnati, OH, USA, 24–27 May 1993. [CrossRef]
44. Chima, R.V. Calculation of Tip Clearance Effects in a Transonic Compressor Rotor. *J. Turbomach.* **1998**, *120*, 131–140. [CrossRef]
45. Suder, K.L.; Celestina, M.L. Experimental and Computational Investigation of the Tip Clearance Flow in a Transonic Axial Compressor Rotor. *J. Turbomach.* **1996**, *118*, 218–229. [CrossRef]